Numerical simulation of interface waves by high-order spectral modeling techniques

Enrico Priolo, José M. Carcione, and Géza Seriani
Osservatorio Geofisico Sperimentale, P.O. Box 2011, Opicina, 34016 Trieste, Italy

(Received 3 June 1993; accepted for publication 1 October 1993)

Few problems in elastodynamics have a closed-form analytical solution. The others can be investigated with semianalytical methods, but in general one is not sure whether these methods give reliable solutions. The same happens with numerical techniques: for instance, finite difference methods solve, in principle, any complex problem, including those with arbitrary inhomogeneities and boundary conditions. However, there is no way to verify the quantitative correctness of the solutions. The major problems are stability with respect to material properties, numerical dispersion, and the treatment of boundary conditions. In practice, these problems may produce inaccurate solutions. In this paper, the study of complex problems with two different numerical grid techniques in order to cross-check the solutions is proposed. Interface waves, in particular, are emphasized, since they pose the major difficulties due to the need to implement boundary conditions. The first method is based on global differential operators where the solution is expanded in terms of the Fourier basis and Chebyshev polynomials, while the second is the spectral element method, an extension of the finite element method that uses Chebyshev polynomials as interpolating functions. Both methods have spectral accuracy up to approximately the Nyquist wave number of the grid. Moreover, both methods implement the boundary conditions in a natural way, particularly the spectral element algorithm. We first solve Lamb's problem and compare numerical and analytical solutions; then, the problem of dispersed Rayleigh waves, and finally, the two-quarter space problem. We show that the modeling algorithms correctly reproduce the analytical solutions and yield a perfect matching when these solutions do not exist. The combined modeling techniques provide a powerful tool for solving complex problems in elastodynamics.

PACS numbers: 43.20.Fn, 43.20.Hq, 43.20.Ks

INTRODUCTION

In geophysical problems, it is important to properly simulate the different types of waves generated at interfaces, as for instance, Rayleigh waves at the surface and Stoneley waves propagating between geological formations. Lamb's problem,[1] i.e., the response of an elastic half-space bounded by a free surface to an impulsive force, has an analytical solution, but others, like the propagation of surface waves in wedge surfaces, or the problem of a quarter-space and two welded quarter-spaces, are difficult if not impossible to attack with analytical methods. They present very complex and interesting phenomena, such as diffractions at corners, and mode coupling and conversion, which generate Rayleigh and interface waves, and whose behavior is very dependent on the material properties. Even Lamb's problem, after many years of research, has not been completely unraveled (for example, the behavior of the non-geometrical modes, and extension to complex rheologies[2]).

To ensure reliable results, a modeling technique has to take care of various aspects, namely, accuracy, proper simulation of boundary conditions, and the ability to model surface topography and irregular interfaces. Accuracy depends mostly on the spatial approximation. Low-order finite element and finite difference schemes have the problem of spatial numerical dispersion. Even fourth-order differential operators do not simulate Rayleigh waves properly, in part due to numerical dispersion and in part because the implementation of the free-surface condition is less accurate than the solution in the interior regions of the model.[3–5] This work presents two different approaches to simulating surface and interface waves in elastic media. The techniques are both based on a Chebyshev expansion of the wave field. The first algorithm solves the elastodynamic equations in differential form by computing the spatial derivatives with the Fourier and Chebyshev pseudospectral methods. The second algorithm uses the Chebyshev polynomials as an interpolant basis in a variational formulation, and is called the Spectral Element Method. Both techniques possess spectral accuracy and are suitable for treating interface problems, particularly the second, for which boundary conditions and arbitrary interface geometries are naturally taken into account. The reason for using two different approaches is for cross-checking the results. Most wave propagation problems have no analytical solution, and if two different techniques give the same solution, one is sure that this solution is free of numerical artifacts.

This paper is organized as follows: the first two sections describe the modeling algorithms, namely, the spatial

 0001-4966/94/95(2)/681/13/$6.00

approximation and the time integration techniques. The numerical simulations are given in Secs. III, IV, and V. The first example compares numerical and analytical solutions of Rayleigh waves propagating along the surface of an homogeneous half-space. This test confirms the accuracy of the numerical algorithms. The second example simulates the dispersed train of Rayleigh waves caused by a surface layer overlying an elastic half-space. Finally, the last simulation compares the numerical results of an interface wave generated by a Rayleigh wave at a vertical interface touching the surface (two-quarter-spaces problem).

I. GLOBAL PSEUDOSPECTRAL METHOD (GPM)

The pseudospectral modeling scheme used in this work was first introduced by Kosloff *et al.*[6] for the elastic wave equation. For computing spatial derivatives, the scheme is based on the Fourier and Chebyshev differential operators in the horizontal and vertical directions, respectively. These operators have infinite accuracy (within machine precision) up to two points per wavelength (the Nyquist wave number) and π points per wavelength, respectively. To balance spatial accuracy, the modeling uses fourth-order time integration techniques, like for instance, the Runge–Kutta method or Taylor expansion of the evolution operator. The modeling scheme developed by Kosloff *et al.* has been extended to the isotropic-viscoelastic rheology by Carcione[7] and to the anisotropic-elastic case by Tessmer *et al.*[8] However, in this paper we will restrict our analysis to elastic surface and interface waves. For completeness, the following subsections briefly describe the modeling algorithm.

A. The wave equation

The wave equation is based on the equation of momentum conservation combined with the constitutive relations for two-dimensional (2-D) isotropic and elastic media.[9] The boundary treatment requires a velocity-stress formulation which takes the following matrix form:

$$\frac{\partial \mathbf{v}}{\partial t}=\mathbf{A}\frac{\partial \mathbf{v}}{\partial x}+\mathbf{B}\frac{\partial \mathbf{v}}{\partial y}+\mathbf{s}, \tag{1}$$

where

$$\mathbf{v}^{\mathrm{T}}=[v_x,v_y,\sigma_{xx},\sigma_{yy},\sigma_{xy}], \tag{2a}$$

is the vector of unknown variables,

$$\mathbf{s}^{\mathrm{T}}=[f_x,f_y,0,0,0] \tag{2b}$$

and

$$\mathbf{A}=\begin{bmatrix}0 & 0 & \rho^{-1} & 0 & 0\\ 0 & 0 & 0 & 0 & \rho^{-1}\\ E & 0 & 0 & 0 & 0\\ \lambda & 0 & 0 & 0 & 0\\ 0 & \mu & 0 & 0 & 0\end{bmatrix},$$

$$\mathbf{B}=\begin{bmatrix}0 & 0 & 0 & 0 & \rho^{-1}\\ 0 & 0 & 0 & \rho^{-1} & 0\\ 0 & \lambda & 0 & 0 & 0\\ 0 & E & 0 & 0 & 0\\ \mu & 0 & 0 & 0 & 0\end{bmatrix}, \tag{3}$$

where $E=\lambda+2\mu$, with $\lambda(\mathbf{x})$ and $\mu(\mathbf{x})$ the Lamé constants. In the preceding equations, $\mathbf{x}=(x,y)$ are the Cartesian coordinates, $v_x(\mathbf{x},t)$ and $v_y(\mathbf{x},t)$ are the particle velocities, $\sigma_{xx}(\mathbf{x},t)$, $\sigma_{yy}(\mathbf{x},t)$, and $\sigma_{xy}(\mathbf{x},t)$ are the stress components, $\rho(\mathbf{x})$ denotes the density, and $\mathbf{f}(\mathbf{x},t)=(f_x,f_y)$ are the body forces per unit volume. The superscript T denotes the transpose of a vector or matrix.

B. Spatial differentiation and boundary conditions

The field variables forming vector v in Eq. (2) are expanded in terms of a finite sequence of orthogonal functions (truncated series) $\{\phi_l\}$ as

$$u=\sum \tilde{u}_l\phi_l. \tag{4}$$

In the x direction we use the set of trigonometric functions

$$\phi_l(x_j)=e^{ik_lx_j}, \tag{5}$$

where the discrete distance and wave number are

$$x_j=jdx, \quad j=0,\ldots,N_x-1 \tag{6}$$

and

$$k_l=\frac{2\pi l}{N_x dx}, \quad l=-\frac{N_x}{2},\ldots,\frac{N_x}{2}-1, \tag{7}$$

respectively, with N_x the number of grid points, and dx the (uniform) grid spacing. The transform pair is

$$\begin{cases}\tilde{u}_l=\dfrac{1}{N_x}\displaystyle\sum_{j=0}^{N_x-1}u_j e^{-2\pi ijl/N_x},\\[2ex] u_j=\displaystyle\sum_{l=-N_x/2}^{N_x/2-1}\tilde{u}_l e^{2\pi ijl/N_x}.\end{cases} \tag{8}$$

Differentiation of u is done in the wave number domain by simply multiplying each Fourier coefficient by the corresponding wave number. The expansion equations (8), are evaluated by using the fast Fourier transform (FFT). In short, the differentiation process is

$$u \overset{\mathrm{FFT}}{\rightarrow} \tilde{u} \rightarrow ik\tilde{u}=\frac{\widetilde{\partial u}}{\partial x} \overset{\mathrm{FFT}^{-1}}{\rightarrow} \frac{\partial u}{\partial x}. \tag{9}$$

In the vertical direction we have to distinguish between computational domain and physical domain. The former is defined by the Gauss–Lobatto points which are densely concentrated at the boundaries of the mesh. Directly computing the solution in this domain requires time steps of the order $O(N_y^{-2})$, making the algorithm highly inefficient. This problem is solved by a mapping transformation of the collocation points such that in the physical domain the minimum grid size is $O(N_y^{-1})$. This transformation reduces the computer time by one order of magnitude.[10]

In the y direction the basis functions are

$$\phi_l(y_j)=T_l(y_j)=\cos(l \arccos y_j), \tag{10}$$

where $T(y)$ are Chebyshev polynomials. In this case, the grid points are defined by

$$y_j=\left(\frac{g(\eta_j)-g(1)}{g(-1)-g(1)}\right)y_{\max}, \tag{11}$$

where

$$\eta_j=\cos\frac{\pi j}{N_y}, \quad j=0,\ldots,N_y \tag{12}$$

are the Gauss–Lobatto collocation points, and g is a mapping transformation given by

$$g(\eta)=-|r|^{-1/2}\arcsin\left(\frac{2r\eta+s}{\sqrt{s^2-4r}}\right), \tag{13}$$

where $r=0.5\alpha^{-2}(\beta^{-2}+1)-1$ and $s=0.5\alpha^{-2}(\beta^{-2}-1)$. Since

$$\frac{d\eta}{dg}=\sqrt{1+s\eta+r\eta^2}, \tag{14}$$

it can be seen that the amount of grid stretching at $\eta=-1$ is $dg/d\eta=\alpha$, and that the stretching at $\eta=1$ is $dg/d\eta=\alpha\beta$. The Gauss–Lobatto points have a maximum spacing at the center of the grid equal to $dy_{\max}=0.5y_{\max}/\sin(\pi/N_y)$ which is conserved by the mapping transformation $g(\eta)$. Note that this coordinate transformation implies that we are no longer using a polynomial approximation for the solution in the physical space. In the computational space, the transform pair is

$$\tilde{u}_l=\frac{2}{N_y\bar{c}_l}\sum_{j=0}^{N_y}\frac{1}{\bar{c}_j}u_j\cos\frac{\pi jl}{N_y}, \tag{15}$$

$$u_j=\sum_{l=0}^{N_y}\tilde{u}_l\cos\frac{\pi jl}{N_y}, \tag{15}$$

where

$$\bar{c}_j=\begin{cases}2, & j=0 \text{ or } N_y\\ 1, & 1\leqslant j\leqslant N_y-1.\end{cases} \tag{16}$$

The spatial derivative of a field variable in the physical domain is then given by

$$\frac{\partial u}{\partial y}=\frac{\partial u}{\partial\eta}\frac{d\eta}{dy}=\left(\frac{g(-1)-g(1)}{y_{\max}}\right)\frac{d\eta}{dg}\frac{\partial u}{\partial\eta}. \tag{17}$$

The first-order derivative of u in the computational domain can be deduced from the following recurrence relation:

$$2T_l=\frac{1}{l+1}T'_{l+1}-\frac{1}{l-1}T'_{l-1}, \quad j\geqslant 1. \tag{18}$$

Assuming that

$$\frac{\partial u}{\partial\eta}=\sum_{j=0}^{N_y}\tilde{u}_l^{(1)}T_l, \tag{19}$$

from Eqs. (15) and (18) we get

$$c_l\tilde{u}_l^{(1)}=\tilde{u}_{l+2}^{(1)}+2(l+1)\tilde{u}_{l+1}, \quad 0\leqslant l\leqslant N_y-1, \tag{20}$$

$$c_l=\begin{cases}2, & \text{if } l=0\\ 1, & \text{if } l\geqslant 1.\end{cases} \tag{21}$$

Since $\tilde{u}_l^{(1)}=0$ for $l\geqslant N_y$, Eq. (20) gives an efficient way of computing the derivative coefficients in decreasing order. The transforms [Eqs. (15)] can be computed by using the FFT algorithm. A more detailed analysis of these differential operators, together with the FORTRAN codes, can be found in the book by Canuto *et al.*[11]

The Chebyshev operator allows the implementation of arbitrary boundary conditions. Each time the right-hand side of Eq. (1) is computed, the boundary conditions are implemented. However, a direct application of these conditions gives unstable solutions. This problem is solved by decomposing the wave field into one-way modes (or characteristics) perpendicular to the boundaries, and modifying these modes according to the boundary conditions. This process implies that for every time step the vector of field variables are modified at the boundary according to the following equations (Kosloff *et al.*[6,12,13]): at the free surface (upper boundary),

$$v_x^{(\text{new})}=v_x^{(\text{old})}+\frac{1}{Z_S}\sigma_{xy}^{(\text{old})}, \quad v_y^{(\text{new})}=v_y^{(\text{old})}+\frac{1}{Z_P}\sigma_{yy}^{(\text{old})},$$
$$\sigma_{xx}^{(\text{new})}=\sigma_{xx}^{(\text{old})}-\frac{\lambda}{E}\sigma_{yy}^{(\text{old})}, \quad \sigma_{yy}^{(\text{new})}=0, \quad \sigma_{xy}^{(\text{new})}=0, \tag{22}$$

where $Z_P=\sqrt{(\lambda+2\mu)\rho}$ and $Z_S=\sqrt{\mu\rho}$ are the compressional and shear impedances of the medium. At the bottom (open radiation condition),

$$v_x^{(\text{new})}=\frac{1}{2}\left(v_x^{(\text{old})}-\frac{1}{Z_S}\sigma_{xy}^{(\text{old})}\right),$$
$$v_y^{(\text{new})}=\frac{1}{2}\left(v_y^{(\text{old})}-\frac{1}{Z_P}\sigma_{yy}^{(\text{old})}\right),$$
$$\sigma_{xx}^{(\text{new})}=\sigma_{xx}^{(\text{old})}-\frac{\lambda}{2E}(\sigma_{yy}^{(\text{old})}+Z_Pv_y^{(\text{old})}), \tag{23}$$
$$\sigma_{yy}^{(\text{new})}=\tfrac{1}{2}(\sigma_{yy}^{(\text{old})}-Z_Pv_y^{(\text{old})}),$$
$$\sigma_{xy}^{(\text{new})}=\tfrac{1}{2}(\sigma_{xy}^{(\text{old})}-Z_Sv_x^{(\text{old})}).$$

Since for nonvertical incidence the incoming waves may not be eliminated completely, an absorbing strip is added to improve the efficiency.[14] Similar absorbing regions are placed along the boundaries in the horizontal direction to avoid wraparound caused by the periodic properties of the Fourier method.

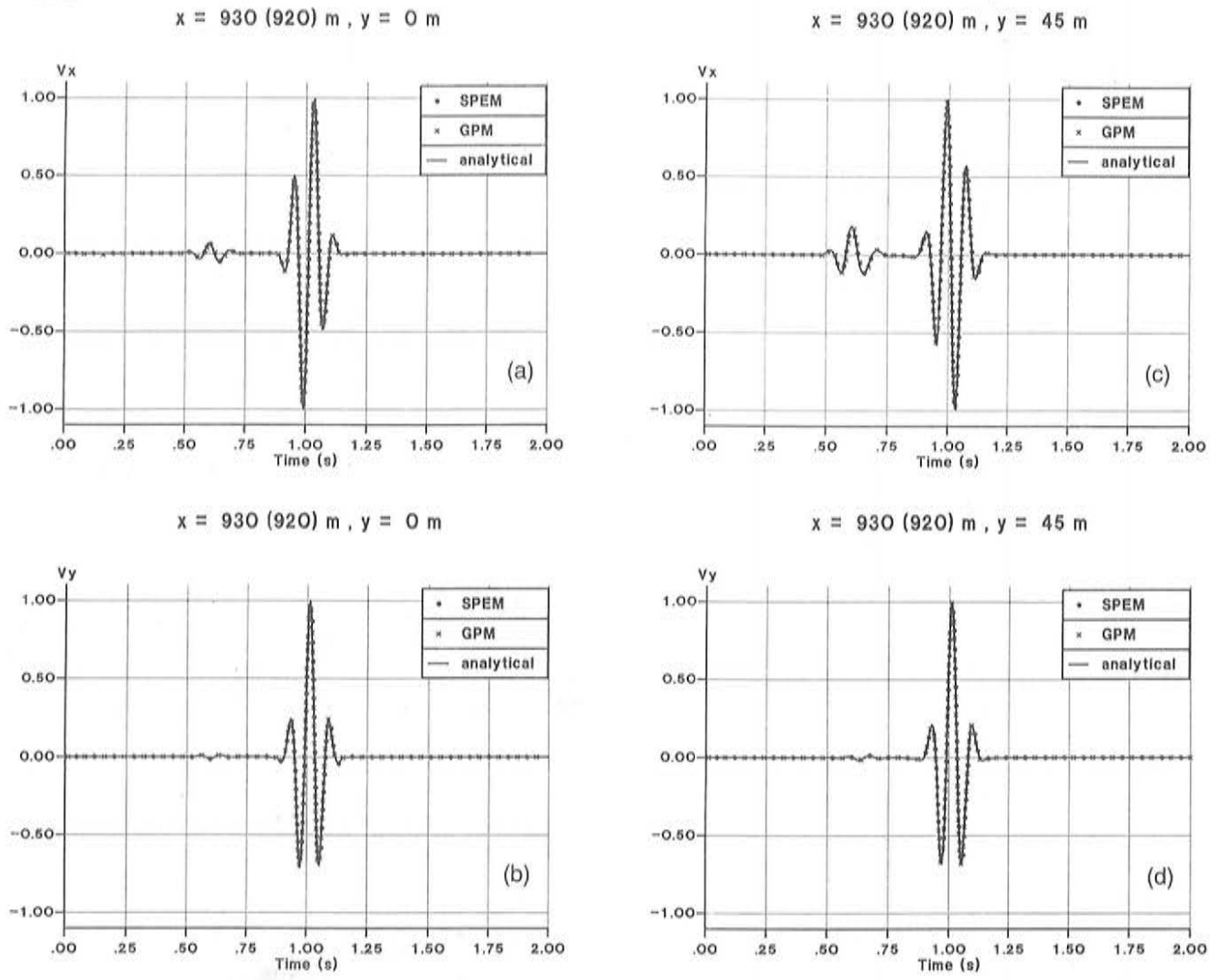

FIG. 1. Lamb's problem. Comparison between analytical and numerical solutions, where (a) and (c) correspond to the v_x component, and (b) and (d) correspond to the v_y component. The coordinates give the position of the receivers relative to the source (the value between parentheses refers to the GPM modeling). The leading pulse is the compressional wave followed by the Rayleigh wave.

The wave field is propagated in time by means of a fourth-order Runge–Kutta method, whose details can be found in Carcione.[7] As mentioned before, a favorable stability condition is achieved with $dt=O(N^{-1})$.

II. SPECTRAL ELEMENT METHOD (SPEM)

The Spectral Element Method (SPEM) is a high-order finite element technique. Priolo and Seriani,[15] and Seriani and Priolo[16,17] first developed and investigated the method for the acoustic wave equation, and Seriani *et al.*[18] extended the modeling to the elastic wave equation. In this work, we decompose the physical domain into rectangular subdomains, where the solution is expressed by a truncated expansion of Chebyshev polynomials. As in the global modeling, the SPEM is practically free of spatial numerical dispersion. The number of grid points per minimum wavelength depends on the degree of the polynomial; for instance, degree 8 resolves 4.6 points per minimum wavelength (note that low-order finite element and standard finite difference schemes need from 15 to 30 points per wavelength). The modeling algorithm is described in the subsections that follow.

A. The wave equation

Let us denote the physical domain by Ω and its boundary by Γ, and express, for brevity, the partial derivatives with respect to x and y by ∂_x and ∂_y, respectively. Using abbreviated subscript notation we define the differential operator

$$\mathbf{D}=\begin{bmatrix}\partial_x & 0\\ 0 & \partial_y\\ \partial_y & \partial_x\end{bmatrix}. \tag{24}$$

Then, the equation of motion, in terms of the displacement field $\mathbf{u}(\mathbf{x},t)$, can be written as

$$\rho\frac{\partial^2\mathbf{u}}{\partial t^2}-\mathbf{D}^{\mathrm{T}}\boldsymbol{\sigma}(\mathbf{u})=\mathbf{f}, \tag{25}$$

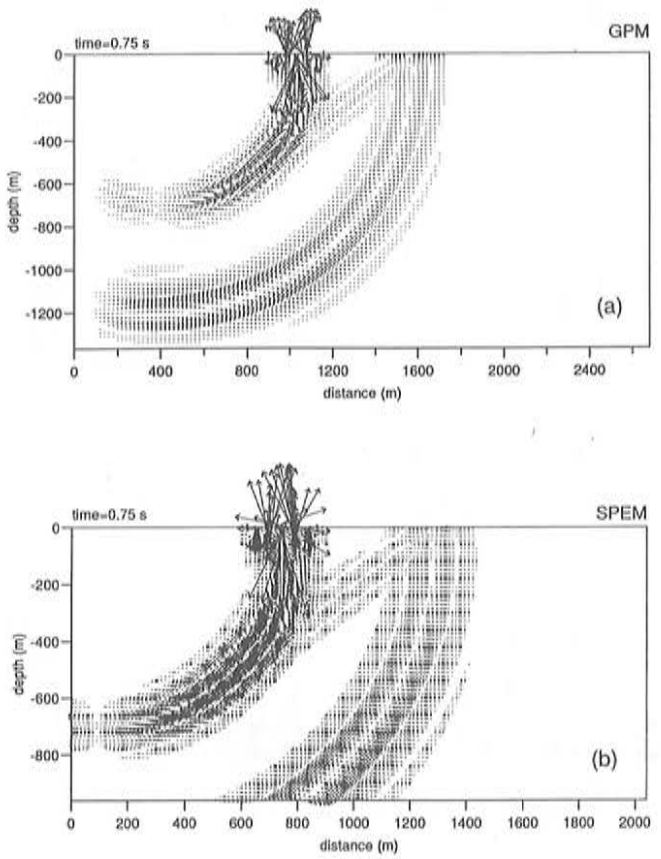

FIG. 2. Lamb's problem. Snapshots of the particle velocity vector at 0.75 s, where (a) is the GPM simulation and (b) is the SPEM simulation. Since the vector is plotted at the grid points, it is evident from the pictures the distribution of the grid points, in particular, the size and distribution of the single elements (each containing 7×7 nodes) in the SPEM snapshot.

where

$$\sigma^{\mathrm{T}}=[\sigma_{xx},\sigma_{yy},\sigma_{xy}] \tag{26}$$

is the stress vector. The stress–strain relation is

$$\sigma(\mathbf{u})=\mathbf{C}\epsilon(\mathbf{u}), \tag{27}$$

where

$$\epsilon^{\mathrm{T}}=[\epsilon_{xx},\epsilon_{yy},\epsilon_{xy}] \tag{28}$$

is the strain vector and $\mathbf{C}$ is the elastic stiffness matrix given by

$$\mathbf{C}=\begin{bmatrix} E & \lambda & 0 \\ \lambda & E & 0 \\ 0 & 0 & \mu \end{bmatrix}. \tag{29}$$

The components of the strain vector are related to the displacement field by

$$\epsilon(\mathbf{u})=\mathbf{D}\mathbf{u}. \tag{30}$$

If we look for sufficiently regular solutions $\mathbf{u}$, and no forces are imposed on the boundary, an equivalent variational formulation of Eq. (25) is to find the solution $\mathbf{u}(\mathbf{x},t)$ of

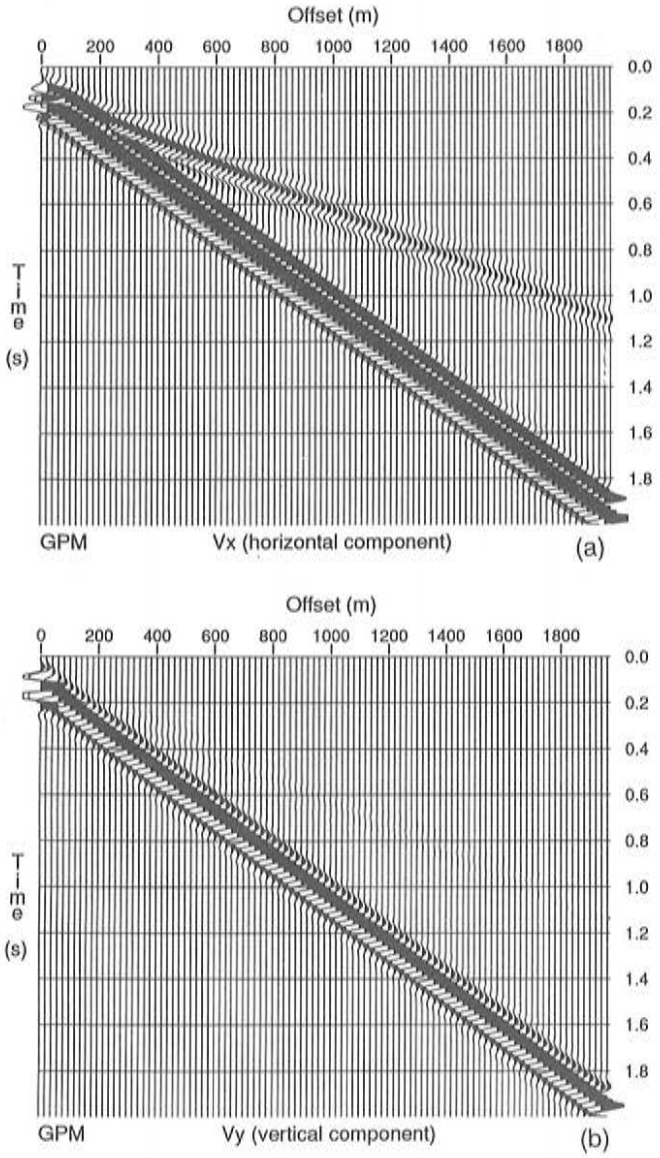

FIG. 3. Lamb's problem. Seismograms recorded at the surface corresponding to the GPM modeling algorithm, where (a) is the v_x component and (b) is the v_y component. The coherent events are the compressional and Rayleigh waves. The SPEM seismograms are completely identical and for this reason are not represented.

$$\frac{d^2}{dt^2}(\mathbf{w},\rho\mathbf{u})_\Omega+a(\mathbf{w},\mathbf{u})_\Omega=(\mathbf{w},\mathbf{f})_\Omega, \tag{31}$$

for all weight functions $\mathbf{w}(\mathbf{x})$ which vanish on the boundary Γ, and which, together with their first derivatives, are square integrable over Ω. The quantities $a(\cdot,\cdot)_\Omega$ and $(\cdot,\cdot)_\Omega$ are symmetric, bilinear forms defined by

$$(\mathbf{w},\rho\mathbf{u})_\Omega=\int_\Omega \rho\mathbf{w}^{\mathrm{T}}\cdot\mathbf{u}\,d\Omega, \tag{32}$$

$$a(\mathbf{w},\mathbf{u})_\Omega=\int_\Omega \epsilon(\mathbf{w})^{\mathrm{T}}\sigma(\mathbf{u})d\Omega=\int_\Omega \mathbf{w}^{\mathrm{T}}\mathbf{D}^{\mathrm{T}}\mathbf{C}\mathbf{D}\mathbf{u}\,d\Omega, \tag{33}$$

$$(\mathbf{w},\mathbf{f})_\Omega=\int_\Omega \mathbf{w}^{\mathrm{T}}\cdot\mathbf{f}\,d\Omega, \tag{34}$$

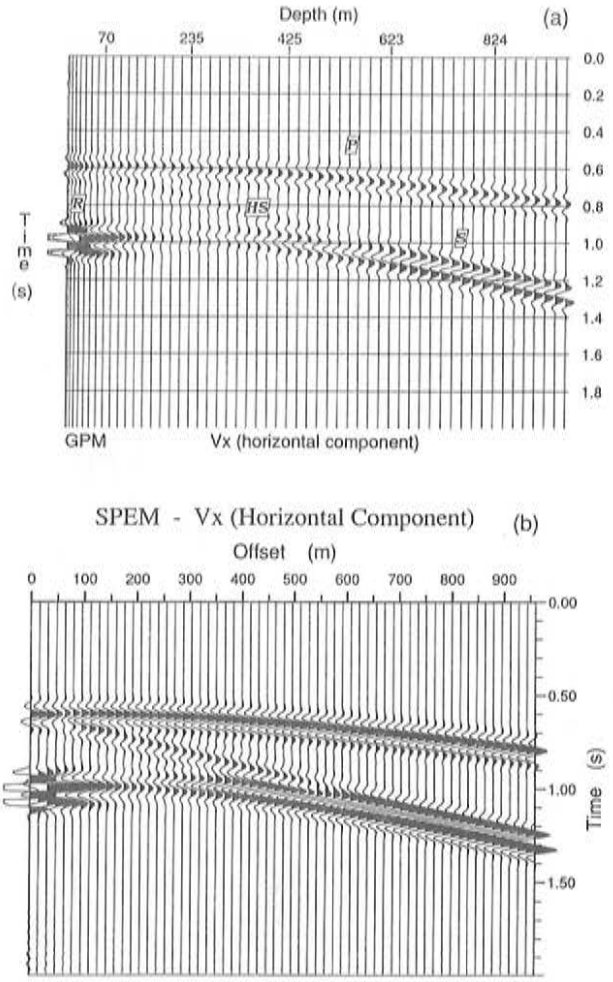

FIG. 4. Lamb's problem. Vertical seismograms (VSP) recorded at a distance of 930 m from the source, corresponding to the GPM modeling (a) and SPEM modeling (b) techniques. The symbols R, P, S, and HS stand for Rayleigh, compressional, shear, and head shear waves, respectively.

where Eqs. (27) and (30) have been used.

B. Discretization of the physical domain

We decompose the physical domain Ω into nonoverlapping quadrilateral elements Ω_e, where $e=1,...,n_e$, with n_e the total number of elements. Let us denote the decomposition of Ω by $\tilde{\Omega}$. On each element, the field is approximated by Chebyshev polynomials of degree N in both coordinates x and y. A function $u(\xi)=u(\xi,\eta)$, defined on the square interval $[-1,1]\times[-1,1]$, can be approximated by a truncated expansion using the following tensor product of Chebyshev polynomials:

$$\tilde{u}(\xi)=\sum_{i=0}^{N}\sum_{j=0}^{N}\tilde{u}_{ij}\varphi_i(\xi)\varphi_j(\eta)\equiv\sum_{i=0}^{N}\sum_{j=0}^{N}\tilde{u}_{ij}\phi_{ij}(\xi), \tag{35}$$

where $\tilde{u}_{ij}=u(\xi_{ij})$ are the values of u at the grid points, and $\varphi_i(\zeta)$ are Lagrangian interpolants satisfying the relation $\varphi_i(\zeta_k)=\delta_{ik}$ within the interval $[-1,1]$ and identically zero outside. Here, δ_{ik} denotes the Kronecker delta symbol and ζ stands for ξ or η. The Lagrangian interpolants are given by

$$\varphi_i(\zeta)=\frac{2}{N}\sum_{p=0}^{N}\frac{1}{\bar{c}_i\bar{c}_p}T_p(\zeta_i)T_p(\zeta), \tag{36}$$

where T_p are the Chebyshev polynomials, ζ_i are the Chebyshev Gauss–Lobatto quadrature points $\zeta_i=\cos(\pi i/N)$ for $i=0,...,N$, and $\bar{c}_i$ is defined in Eq. (16). The coordinates $\xi_{ij}=\{\xi_i,\eta_j\}$ of the internal nodes for the discretization of the quadrilateral domain $[-1,1]\times[-1,1]$ are obtained as Cartesian products of the ζ_i points. In order to apply these interpolants and construct the approximating function space, we need to define the mapping $\Lambda^{(e)}(\mathbf{x}):\mathbf{x}\in\Omega_e\rightarrow\xi^{(e)}\in[-1,1]^2$ between the points $\mathbf{x}\in[a_e,a_{e+1}]\times[b_e,b_{e+1}]$ of each element Ω_e of the decomposition $\tilde{\Omega}$ in the physical domain and the local element coordinate system $\{\xi,\eta\}$ by

$$\Lambda^{(e)}(\mathbf{x})\equiv\{\xi^{(e)},\eta^{(e)}\}=\left\{\frac{2}{\Delta_x^e}(x-a_e)-1,\frac{2}{\Delta_y^e}(y-b_e)-1\right\}, \tag{37}$$

with $\Delta_x^e=a_{e+1}-a_e$ and $\Delta_y^e=b_{e+1}-b_e$ the dimensions of the element Ω_e. Then, the global approximating function is formed by the sum of the elemental approximating functions [Eqs. (35)] defined on each element.

C. Discretization of the wave equation

In the decomposed physical domain $\tilde{\Omega}$ we define the trial functions $\tilde{\mathbf{u}}(\mathbf{x},t)$ and the weight functions $\tilde{\mathbf{w}}(\mathbf{x})$ following the previous approach, and denote with $\tilde{\mathbf{u}}_e$ and $\tilde{\mathbf{w}}_e$ the restrictions to each Ω_e of $\tilde{\mathbf{u}}$ and $\tilde{\mathbf{w}}$, respectively (Seriani *et al.*[18]). It can be shown that the 2D wave propagation problem is equivalent to finding $\tilde{\mathbf{u}}_e$ such that, for all $\tilde{\mathbf{w}}_e$, the following equations are satisfied on each element Ω_e:

$$\frac{d^2}{dt^2}(\tilde{\mathbf{w}}_e,\rho\tilde{\mathbf{u}}_e)_N+a(\tilde{\mathbf{w}}_e,\tilde{\mathbf{u}}_e)_N=(\tilde{\mathbf{w}}_e,\tilde{f}_e)_N, \tag{38}$$

enforcing the continuity condition for the solution on the element boundaries, and where $a(\cdot,\cdot)_N$ and $(\cdot,\cdot)_N$ are symmetric, bilinear forms computed according to the definitions, Eqs. (32)–(34), at the element level. Using the definition of $\varphi_i(\zeta)$ given in Eq. (36), we compute the derivative matrix $D_{ij}=d\varphi_i(\zeta_j)/d\zeta$ and the semidiscrete differential operator $\mathbf{D}_{ij}$ defined on each element Ω_e by

$$\mathbf{D}\tilde{\mathbf{u}}_e(\xi,t)=\sum_{i=0}^{N}\sum_{j=0}^{N}\mathbf{D}_{ij}\tilde{\mathbf{u}}_{ij}^{(e)}(t). \tag{39}$$

We can now evaluate each term of Eq. (38) using the mapping $\Lambda^{(e)}$ and Eq. (39). Requiring that the variational equation be satisfied for all $\tilde{\mathbf{w}}_e$, the spectral element approximation of the original equation finally yields a set of linear differential equations

$$\mathbf{M}\ddot{\mathbf{U}}+\mathbf{K}\mathbf{U}=\mathbf{F}, \tag{40}$$

with $\mathbf{U}(0)=\{U_0\}$, $\dot{\mathbf{U}}(0)=\{\dot{U}_0\}$ as initial conditions, where the unknown vector $\mathbf{U}$ contains the values of the discrete solution $\tilde{\mathbf{u}}$ at all Chebyshev points

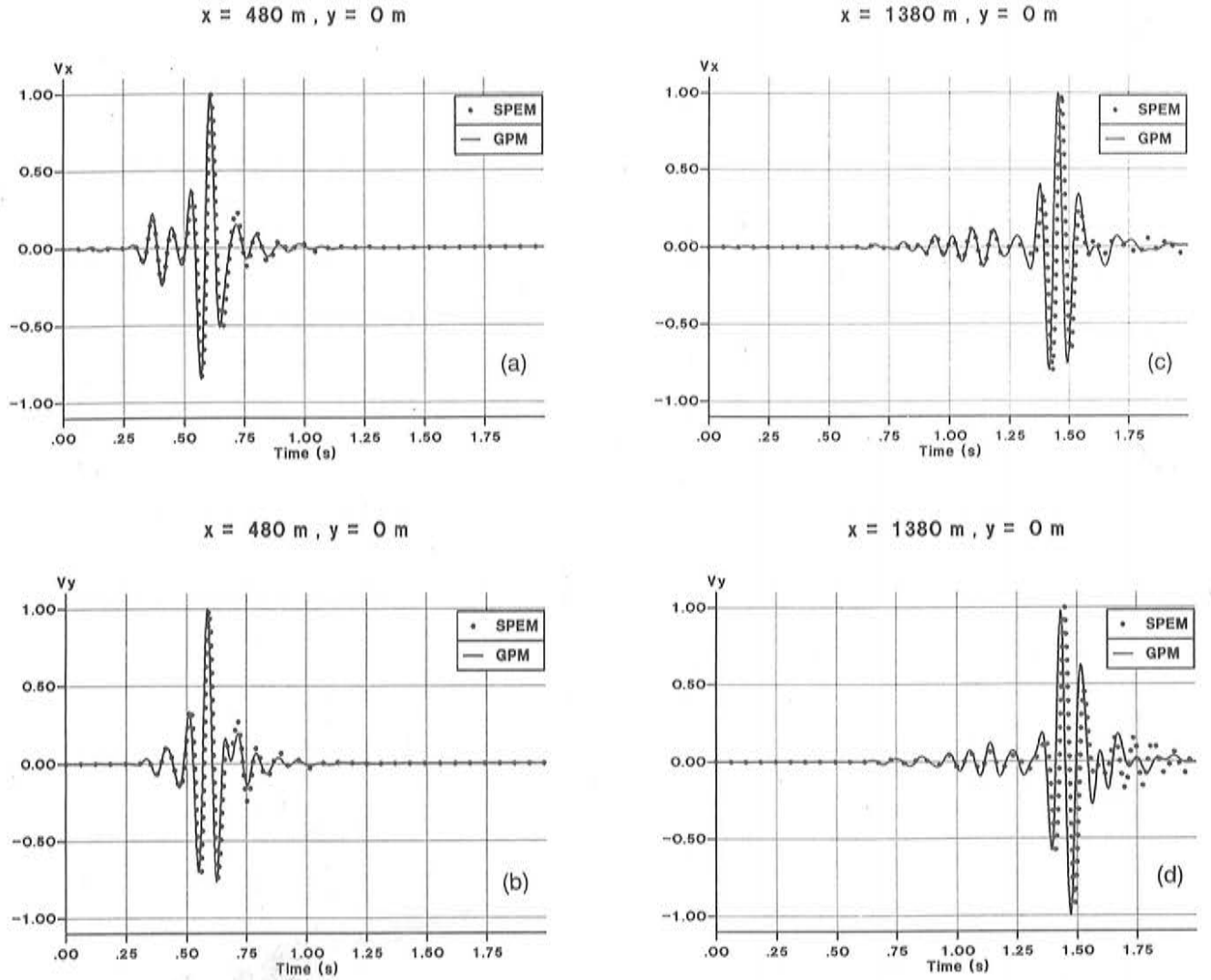

FIG. 5. Dispersed Rayleigh waves problem. Comparison between numerical solutions at different receivers, where (a) and (c) correspond to the v_x component, and (b) and (d) correspond to the v_y component. The position of the solid–solid interface is 123 m from the surface.

$\mathbf{x}_{ij}^{(e)}=[\Lambda^{(e)}]^{-1}\xi_{ij}$ for $i,j=0,\ldots,N$ and for all $e=0,\ldots,n_e$. A dot above a variable denotes time differentiation. In Eq. (40), $\mathbf{M}$ is the mass matrix, $\mathbf{K}$ is the stiffness matrix, and $\mathbf{F}$ is the force vector obtained after a global nodal renumbering and assembly of all the elemental matrices and force vector contributions. They can be computed using the matrix element summation or "stiffness" summation over all the elements of $\mathbf{M}^{(e)}$, $\mathbf{K}^{(e)}$, and $\mathbf{F}^{(e)}$, which are the elemental matrices and force vector, respectively. The contributions from nodes which are common to an element pair are summed to enforce the continuity requirement of the solution on the element boundaries. The elemental mass matrix is given in block form by

$$\mathbf{M}^{(e)}=\begin{bmatrix}\bar{\mathbf{M}}^{(e)} & \mathbf{0}\\ \mathbf{0} & \bar{\mathbf{M}}^{(e)}\end{bmatrix}, \tag{41}$$

where $\mathbf{0}$, the zero matrix, and $\bar{\mathbf{M}}^{(e)}$ have dimension $(N+1)^2\times(N+1)^2$ with

$$[\bar{\mathbf{M}}^{(e)}]_{(ij)(lm)}=\int_{\Omega_e}\phi_{ij}\rho\phi_{lm}\,d\Omega=\frac{\Delta_x^e\Delta_y^e}{4}\rho A_{il}A_{jm}, \tag{42}$$

and the quantities A are given below. The elemental stiffness matrix is given by

$$\mathbf{K}^{(e)}=\int_{\Omega_e}[\mathbf{D}_{ij}^{\mathsf{T}}\mathbf{C}\mathbf{D}_{lm}]d\Omega=\begin{bmatrix}\bar{\mathbf{K}}_1^{(e)} & \bar{\mathbf{K}}_2^{(e)}\\ \bar{\mathbf{K}}_2^{(e)\mathsf{T}} & \bar{\mathbf{K}}_3^{(e)}\end{bmatrix}, \tag{43}$$

where the $(N+1)^2\times(N+1)^2$ submatrices $\bar{\mathbf{K}}^{(e)}$ are

$$\begin{aligned}[\bar{\mathbf{K}}_1^{(e)}]_{(ij)(lm)}&=E\frac{\Delta_y^e}{\Delta_x^e}C_{il}A_{jm}+\mu\frac{\Delta_x^e}{\Delta_y^e}A_{il}C_{jm},\\ [\bar{\mathbf{K}}_2^{(e)}]_{(ij)(lm)}&=\lambda B_{il}B_{mj}+\mu B_{li}B_{jm},\\ [\bar{\mathbf{K}}_3^{(e)}]_{(ij)(lm)}&=E\frac{\Delta_x^e}{\Delta_y^e}A_{il}C_{jm}+\mu\frac{\Delta_y^e}{\Delta_x^e}C_{il}A_{jm},\end{aligned} \tag{44}$$

and $[\bar{\mathbf{K}}_2^{(e)\mathsf{T}}]_{(ij)(lm)}=[\bar{\mathbf{K}}_2^{(e)}]_{(lm)(ij)}$. Finally, the force vectors, of dimension $(N+1)^2$, are given by

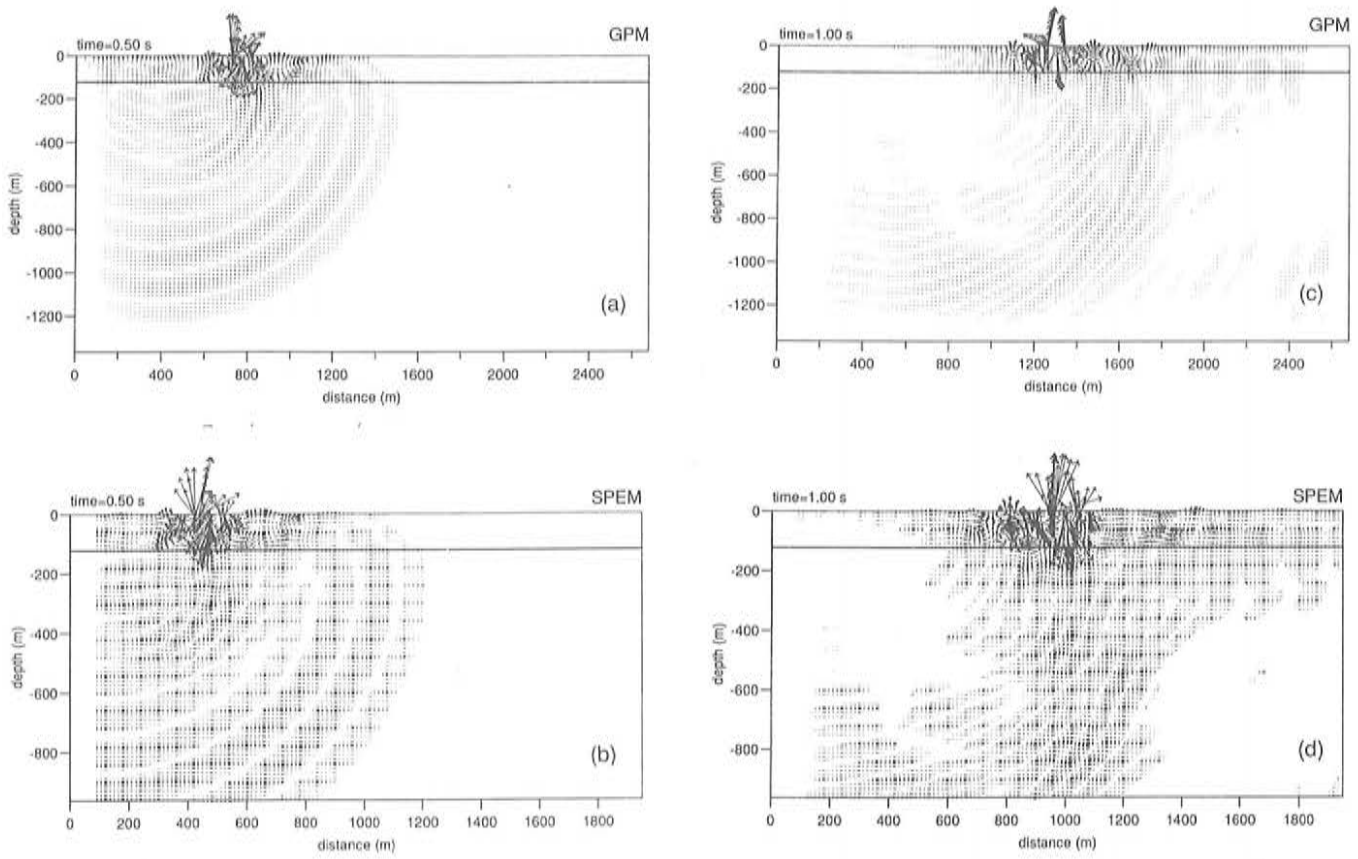

FIG. 6. Dispersed Rayleigh waves problem. Snapshots of the particle velocity vector at two different propagation times, where (a) and (c) are the GPM simulations and (b) and (d) are the SPEM simulations. The propagation displays most of the usual normal-mode characteristics corresponding to a surface layer overlying a solid half-space.

$$\mathbf{F}^{(e)}=\{\mathbf{F}_{ij}^{(e)}\},$$

$$\mathbf{F}_{ij}^{(e)}=\int_{\Omega_e}\phi_{ij}\mathbf{f}\,d\Omega=\frac{\Delta_x^e\Delta_y^e}{4}\sum_{l,m=0}^{N}A_{il}A_{jm}\mathbf{f}_{lm}^e, \tag{45}$$

where $\mathbf{f}_{lm}^e$ are the grid values of the forcing term, and the quantities A, B, and C are defined by

$$A_{ij}=\frac{4}{N^2\bar{c}_i\bar{c}_j}\sum_{p,q=0}^{N}\frac{1}{\bar{c}_p\bar{c}_q}T_p(\xi_i)T_q(\xi_j)\int_{-1}^{1}T_pT_q\,d\xi, \tag{46}$$

$$B_{ij}=\sum_{l=0}^{N}D_{il}A_{jl},\quad C_{ij}=\sum_{l,m=0}^{N}D_{il}D_{jm}A_{lm}. \tag{47}$$

Time integration of Eq. (40) is performed numerically by the implicit Newmark scheme, which is a two-step algorithm, unconditionally stable and second-order accurate.[19] The solution at time $(n+1)dt$ is obtained by solving the sparse, symmetric system of linear equations

$$\left(\mathbf{M}+\frac{dt^2}{4}\mathbf{K}\right)\mathbf{U}^{n+1}=\frac{dt^2}{4}\mathbf{F}^{n+1}+\mathbf{M}\left(\mathbf{U}^n+dt\,\dot{\mathbf{U}}^n+\frac{dt^2}{4}\ddot{\mathbf{U}}^n\right), \tag{48}$$

with the Conjugated Gradient method preconditioned by the Incomplete Cholesky Factorization.[20] Although the method is unconditionally stable, accuracy imposes

$$dt\leqslant\frac{\min(dx,dy)}{\sqrt{3(c_P^2+c_S^2)}}, \tag{49}$$

where dx and dy are the grid spacings in the x and y directions, respectively. Note that the minimum grid spacing occurs at the interval end points of the Chebyshev interpolator, and is given by $d_{\min}\simeq\pi^2\Delta^e/(4N^2)$. Although this spacing is $O(N^{-2})$, it is not very restrictive, since spectral accuracy is achieved with $N\leqslant 8$.

III. LAMB'S PROBLEM

This example verifies the numerical solutions with the analytical solution of Lamb's problem, that is, the response of an elastic half-space bounded by a free surface to an impulsive vertical force.[1] Since Lamb's work, this problem has been investigated by many researchers, in particular, Khun[2] recently published a detailed numerical analysis of the different waves. The global pseudospectral modeling uses a grid size of $N_x=135$ and $N_y=81$, with grid spacings of $dx=20$ m and $dy_{\max}=20$ m. The parameters of the mapping transformation are $\alpha=2.583$ and $\beta=2$, so that the second and third grid points are at 1.01 and 4.02 m from the surface (first grid point), respectively. At the sides and

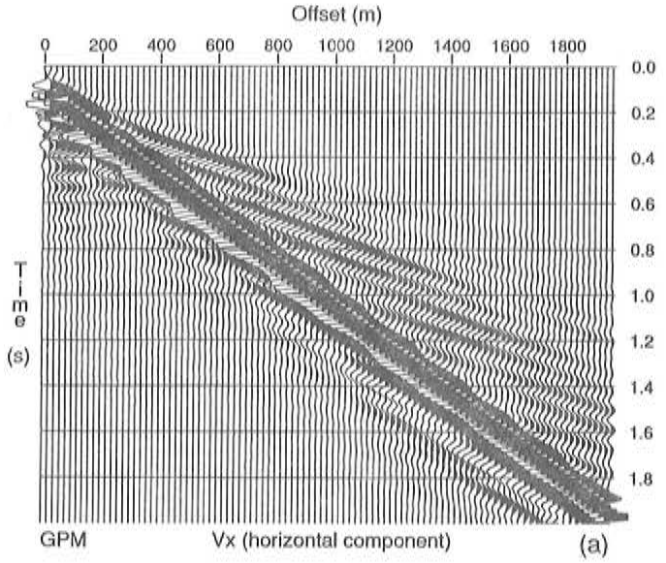

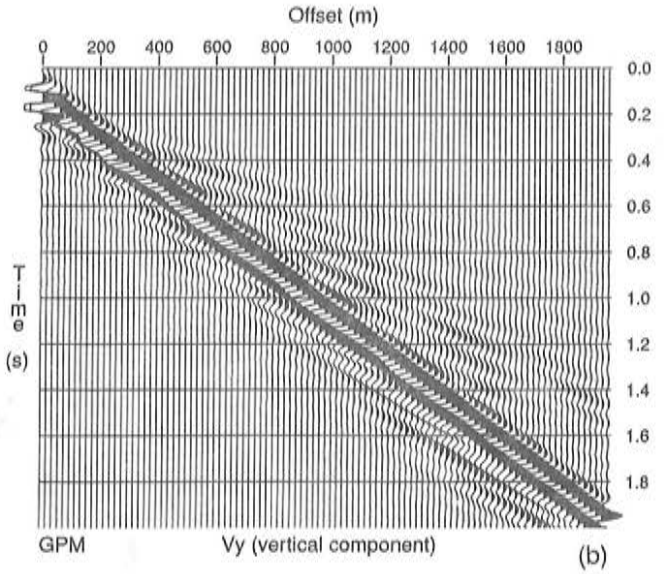

FIG. 7. Dispersed Rayleigh waves problem. Seismograms recorded at the surface corresponding to the GPM modeling algorithm, where (a) is the v_x component and (b) is the v_y component. The main event is the Rayleigh wave which shows velocity dispersion compared to Lamb's problem.

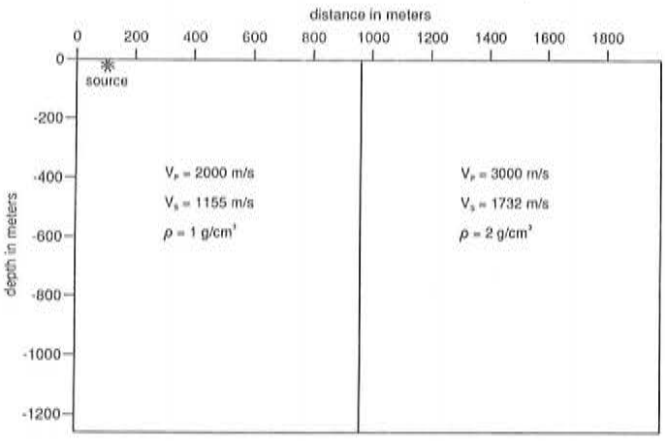

FIG. 8. Two-quarter-spaces problem. Dimensions of the model and material properties.

at the bottom of the mesh, we implement absorbing strips of 18 points length. The numerical solution is propagated to 2 s with a time step of 1 ms.

The SPEM domain is composed of 65×31 elements. Each element has a size of 60 m in the horizontal and vertical directions, and contains 49 nodes defined by the $N+1$ quadrature points of a Chebyshev polynomial of order $N=6$. Considering that the elements have common boundary points, the total number of nodes is 73 117. In practice, the actual model is contained in an inner region bounded by the free surface and composed of 34×16 elements. In the outer region, the elements are gradually stretched towards the boundaries of the computational mesh in order to simulate open radiation conditions. The minimum distance between grid points is 4.02 m, occurring at the interval end point of the elements. This minimum grid size and the material properties impose a time step of 1.25 ms. The source function is given by

$$f_x=0, \quad f_y=\delta(x-x_0)\delta(y-y_0)h(t), \tag{50}$$

where $y_0=4.02$ m (the value of x_0 is not relevant). The time history of the source is

$$h(t)=e^{0.5f_0^2(t-t_0)^2}\cos[\pi(t-t_0)], \tag{51}$$

where $t_0=0.06$ s, and $f_0=22$ Hz is the cutoff frequency. Since the spectral element modeling solves for the displacement field, and the global modeling solves for the time derivative of the displacements, the former uses the time derivative of Eq. (51) as source time history in order to compare both methods. The wave velocities are $c_p=2000$ m/s and $c_s=1155$ m/s, and the density is $\rho=1$ g/cm^3.

Figure 1 compares the numerical solutions with the analytical solutions at two different receivers. The analytical solution is obtained by the Cagniard-de Hoop technique.[21] The coordinates give the position of the receivers relative to the source with the value between parentheses corresponding to the pseudospectral method. This difference is due to the fact that the solutions are computed at different grid points. As can be observed, the matching between the solutions is virtually perfect. The main pulse is the Rayleigh wave and the first event is the compressional wave whose amplitude increases with depth, as can be appreciated from the figures.

Figure 2 compares snapshots of the particle velocity vector at 0.75-s propagation time. The vector is plotted at the grid points. The GPM snapshot includes the absorbing strips where the wave field is attenuated (e.g., the left side) in order to eliminate nonphysical reflections from the boundaries of the mesh. In the SPEM snapshot the size and distribution of nodes of the single elements can be clearly appreciated. The leading wave front corresponds to the compressional wave as can be interpreted from its longitudinal motion and position. Then follows the shear head wave connecting the P wave with the shear wave front, and finally the Rayleigh wave confined near the surface. In Fig.

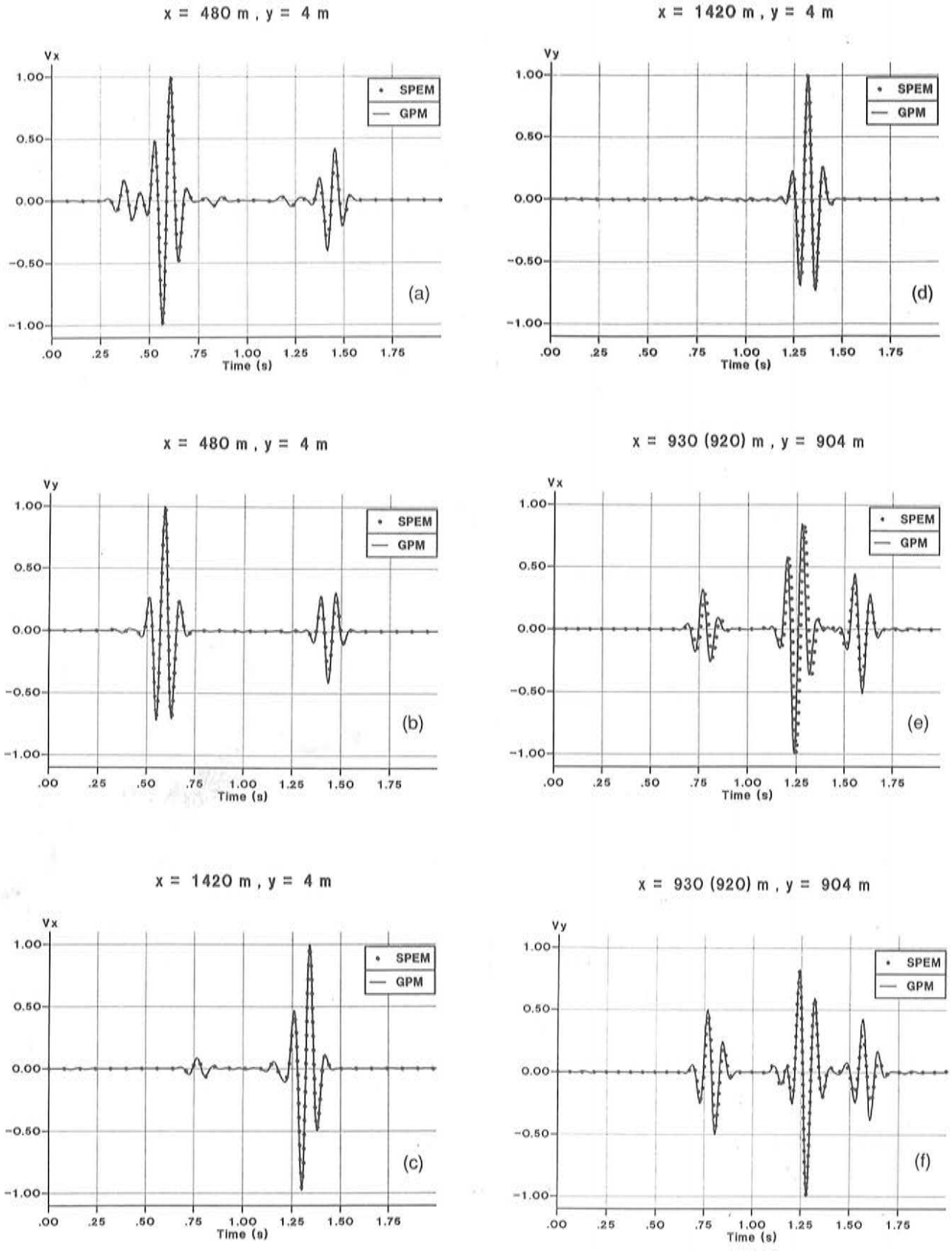

FIG. 9. Two-quarter-spaces problem. Comparison between numerical solutions: (a) and (b), horizontal and vertical components, respectively, in a receiver near the surface and between the source and the vertical interface, where the main and reflected Rayleigh pulses can be observed; (c) and (d), horizontal and vertical components, respectively, in a receiver beyond the interface and near the surface, where the compressional and transmitted Rayleigh waves are the most prominent events; and (e) and (f), horizontal and vertical components, respectively, in a receiver at depth and on the interface, where the first, second and third arrivals correspond to the compressional, shear, and interface waves, respectively.

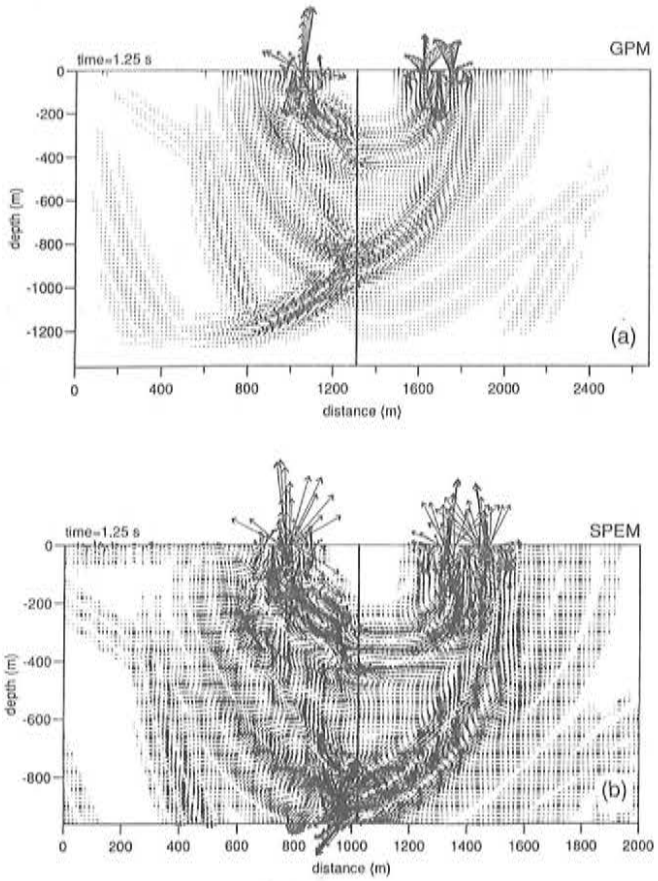

FIG. 10. Two-quarter-spaces problem. Snapshots of the particle velocity vector at 1.25 s corresponding to the GPM (a) and SPEM (b) simulations. The reflected and transmitted Rayleigh waves are the main features at the surface. At depth, the body and interface waves are most prominent. The characteristic elliptical motion of the Rayleigh and interface waves can be clearly appreciated.

3 we show the GPM seismograms recorded at the surface where the compressional and Rayleigh waves can be clearly distinguished. The SPEM seismograms are identical to those of Fig. 3 and for this reason are not shown. The different waves can be appreciated better in the vertical seismograms shown in Fig. 4 and recorded at a distance of 930 m from the source, where the symbols R, P, S, and HS stand for Rayleigh, compressional, shear, and head shear waves, respectively.

IV. DISPERSED RAYLEIGH WAVES PROBLEM

Rayleigh waves are dispersive when a surface layer overlies an elastic half-space.[22] This problem has no analytical solution. Kosloff *et al.*[6] compared their numerical solution with results from a propagator matrix method.[23] However, the match was not good since, as they state, the propagator matrix solution does not account for the body waves, which contribute significant amplitudes, in particular before the arrival of the main Rayleigh pulse.

The thickness of the surface layer is 123 m, and its material properties are $c_p=2000$ m/s, $c_s=1155$ m/s, and $\rho=1$ g/cm^3. The overlying half-space has $c_p=3000$ m/s, $c_s=1500$ m/s, and $\rho=2$ g/cm^3. The numerical mesh, source, source depth, and time step for the global modeling are the same as in Lamb's problem. The position of the layer relative to the surface is defined between the vertical grid points 13 at 115 m, and 14 at 131 m. The SPEM numerical mesh is in general similar to that used for the previous example. The difference is that the elements of the surface layer are stretched to define the interface at 123-m depth.

Figure 5 compares the numerical solutions at two different surface receivers. The solutions are in quite good agreeement. Some differences can be attributed to the fact that the interface in the GPM model is not exactly at 123 m. A more precise definition of the interface with this method can be achieved by using mapping transformations which increase the density of points in the interface. Snapshots of the particle velocity vector at two different propagation times are illustrated in Fig. 6. The propagation displays most of the usual normal-mode characteristics at large distances from the source. Figure 7 illustrates the seismograms recorded at the surface. The fundamental mode corresponds to the Rayleigh wave.

V. THE TWO-QUARTER-SPACES PROBLEM

This problem was first investigated with numerical modeling by Ottaviani,[24] and recently solved by Kosloff *et al.*[6] in the elastic case, and by Carcione[7] in the anelastic case. It consists (see Fig. 8) of a vertical interface in contact with the surface. The focus here is in the process by which the Rayleigh wave, originated by a vertical force, generates an interface wave traveling downwards. The problem has no known analytical solution and constitutes a good test of the modeling algorithms.

The numerical mesh, source, source depth, and time step for the GPM modeling is the same as in Lamb's problem. The SPEM mesh is similar to that of Lamb's problem, the only difference is that the elements of the right quarter-space have a size of 70 m (instead of 60 m), since the wave velocities there are higher than in the left quarter-space.

Figure 9 compares the numerical solutions at three different receivers: (a) near the surface between the source and the interface, (b) near the surface beyond the interface, and (c) at depth on the interface. The GPM solution is computed at 10 m from the vertical interface (for global methods the interfaces are located between grid points). The matching between solutions is excellent; the difference in (c) is due to the different locations of the receivers in both methods. The events at approximately 1.25 s in (a) and (b) are the reflected and transmitted Rayleigh waves, respectively. In (c), the first pulse corresponds to the compressional wave, the second is the shear wave, and the third, at approximately 1.5 s, is an interface wave.

Figure 10 shows snapshots of the particle velocity vector at 1.25 s. The reflected and transmitted Rayleigh waves are the main features at the surface, while the interface wave generated by the incident Rayleigh is traveling downwards along the vertical interface. Surface and vertical seismograms are displayed in Figs. 11 and 12, respectively, the latter along the interface. In Fig. 12 we show the horizontal components of both methods where the interface wave, denoted by the symbol I, is one of the main events. The

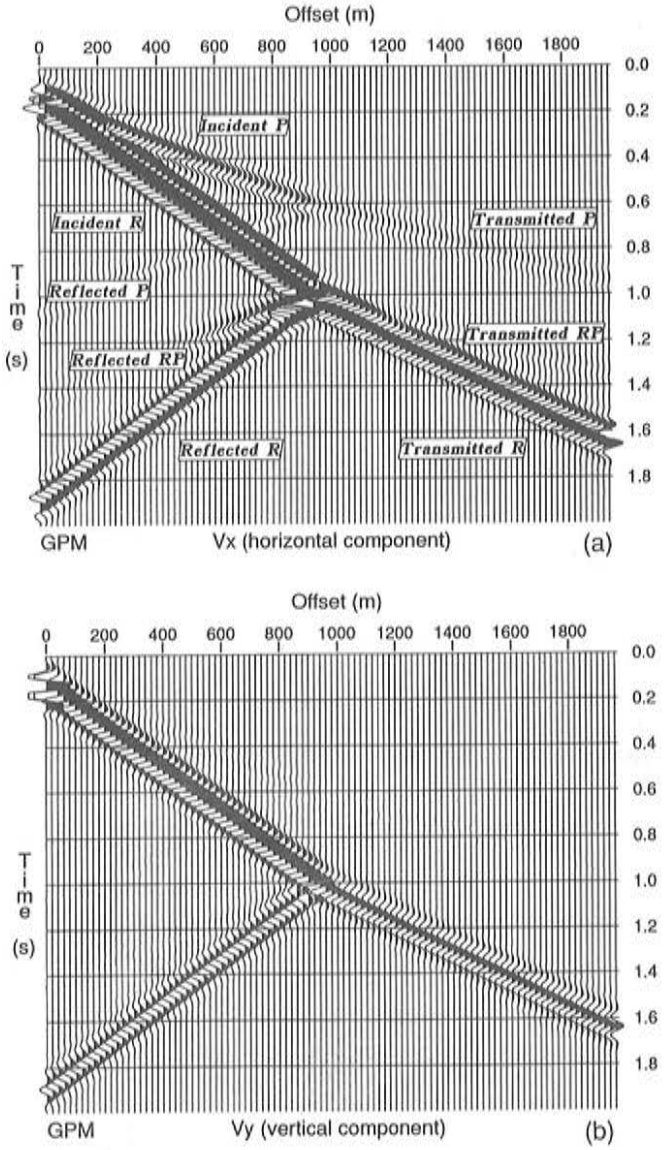

FIG. 11. Two-quarter-spaces problem. Surface seismograms computed with the GPM modeling algorithm, where (a) is the v_x component and (b) is the v_y component. The symbols R and P refer to the Rayleigh and compressional waves, respectively.

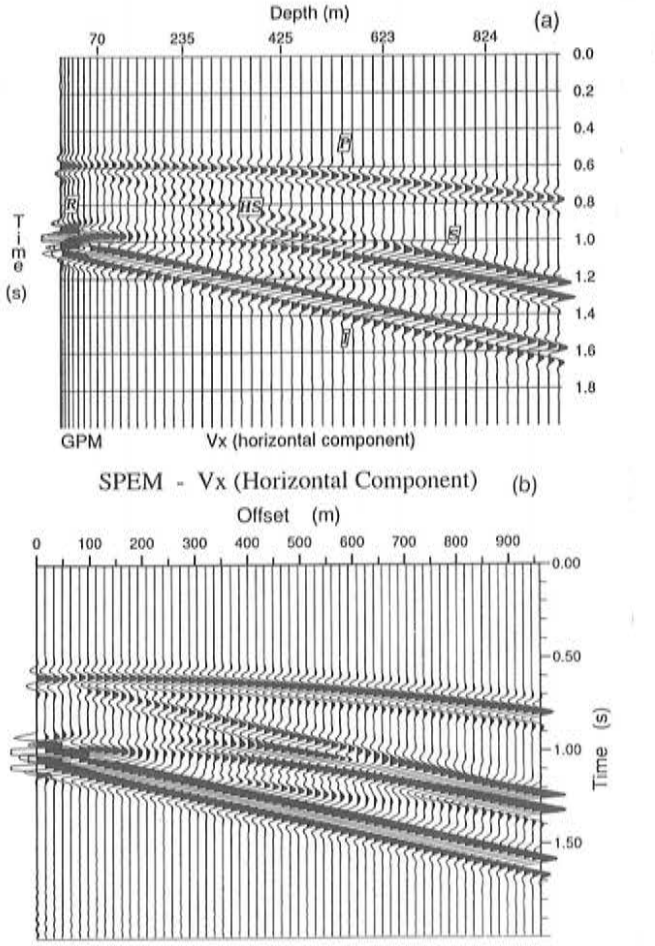

FIG. 12. Two-quarter-spaces problem. Vertical seismograms computed with both techniques, in (a), the GPM modeling, and in (b), the SPEM modeling. The horizontal particle velocity is shown. The interface wave, denoted by the symbol I is one of the main events. The velocity of this wave is approximately 1600 m/s, that is between the shear velocities of the two media.

velocity of this wave is approximately 1600 m/s, which lies between the shear velocities of the two media.

VI. CONCLUSIONS

We have successfully cross-checked two different numerical modeling techniques for solving complex problems in elastodynamics. The GPM is based on explicit differentiation of the field variables, and the SPEM solves a variational formulation. In particular, the two-quarter-spaces problem involves complex phenomena like transmission and reflection of Rayleigh waves, and the generation of interface waves at the welded contact. These modes, which constitute a severe test for the boundary conditions, are correctly reproduced in amplitude and phase. Differences between numerical solutions may be caused by different positions of the interfaces (GPM defines them between grid points and SPEM at grid points) and the receivers. The first problem can be solved by using a 2-D Chebyshev differential operator and mapping transformations in the GPM modeling, or adapting the size of the SPEM elements to the GPM mesh. Comparisons for common receiver points can be solved by interpolating the wave field between grid points.

Of both methods, the more promising is the SPEM algorithm due to its versatility to model complex geometries and boundary conditions. However, at present, the GPM method is more efficient in terms of storage and computer time. This suggests that, in the context of domain decomposition techniques, a hybrid modeling code combining both methods could be highly performing.

Several problems are of immediate interest for investigation. For instance, an analysis of the quarter-space problem (step at the free surface), studied theoretically by Lapwood,[25] and experimentally by Bremaecker[26] and Knopoff and Gangi.[27] This problem requires the use of 2-D Chebyshev differential operators[28] and domain decomposition methods[29] in the global modeling technique. Also, of interest is a detailed study of the two-quarter-space prob-

lem to confront with the numerical seismograms and experimental oscillograms obtained by Ottaviani.[24]

A natural extension of the modeling algorithms involves the use of coordinate transformations,[30] such that the grid points can be adapted to topographic features and curved interfaces. This could allow, for instance, attacking the problem of Rayleigh waves on curved surfaces,[31,32] like the whispering gallery effect.[33]

ACKNOWLEDGMENT

This work was supported in part by the Commission of the European Communities under the GEOSCIENCE project.

[1] H. Lamb, "On the propagation of tremors over the surface of an elastic solid," Philos. Trans. R. Soc. London Ser. A **203**, 1–42 (1904).
[2] M. J. Khun, "A numerical study of Lamb's problem," Geophys. Prospect. **33**, 1103–1137 (1985).
[3] A. Bayliss, K. E. Jordan, B. J. LeMesurier, and E. Turkel, "A fourth-order accurate finite-difference scheme for the computation of elastic waves," Bull. Seismol. Soc. Am. **76**, 1115–1132 (1986).
[4] J. Virieux, "*P-SV* wave propagation in heterogeneous media: Velocity-stress finite-difference method," Geophysics **51**, 889–901 (1986).
[5] A. R. Levander, "Fourth-order finite-difference *P-SV* seismograms," Geophysics **53**, 1425–1436 (1988).
[6] D. Kosloff, D. Kessler, A. Queiroz Filho, E. Tessmer, A. Behle, and R. Strahilevitz, "Solution of the equations of dynamic elasticity by a Chebyshev spectral method," Geophysics **55**, 734–748 (1990).
[7] J. M. Carcione, "Modeling anelastic singular surface waves in the earth," Geophysics **57**, 781–792 (1992).
[8] E. Tessmer and A. Behle, "3D seismic modelling of general material anisotropy in the presence of the free surface by a Chebyshev spectral method," in *Proceedings of the 54th Meeting and Technical Exhibition* (EAEG, Paris, 1992), pp. 134–135.
[9] Y. C. Fung, *Foundations of Solid Mechanics* (Prentice-Hall, Englewood Cliffs, NJ, 1965).
[10] D. Kosloff and H. Tal-Ezer, "A modified Chebyshev pseudospectral method with an $O(N^{-1})$ time step restriction," J. Comp. Phys. **104**, 457–469 (1993).
[11] C. Canuto, M. Y. Hussaini, A. Quarteroni, and T. A. Zang, *Spectral Methods in Fluid Dynamics* (Springer-Verlag, New York, 1988).
[12] J. M. Carcione, "Time-dependent boundary conditions for the 2-D linear anisotropic viscoelastic equation," Numer. Methods Partial Different. Eq. (submitted).
[13] J. M. Carcione, "Boundary conditions for wave propagation problems," in *Spectral and High Order Methods for Partial Differential Equations*, ICOSAHOM '92, Le Corum, edited by C. Bernardi and Y. Maday (North-Holland, Amsterdam, 1994) (in press).
[14] R. Kosloff and D. Kosloff, "Absorbing boundaries for wave propagation problems," J. Comput. Phys. **63**, 363–376 (1986).
[15] E. Priolo and G. Seriani, "A numerical investigation of Chebyshev spectral element method for acoustic wave propagation," in *Proceedings of the 13th World Congress on Computation and Applied Mathematics*, IMACS, Trinity College, Dublin, edited by R. Vichnevetsky and J. J. H. Miller (Criterion, Dublin, 1991), Vol. 2, pp. 551–556.
[16] G. Seriani and E. Priolo, "High-order spectral element method for acoustic wave modelling," Abstracts of the 61st Annual International SEG Meeting, Houston, Texas, Soc. Expl. Geophys. **2**, 1561–1564 (1991).
[17] G. Seriani and E. Priolo, "Spectral element method for acoustic wave simulation in heterogenous media," in Ref. 13.
[18] G. Seriani, E. Priolo, J. M. Carcione and E. Padovani, "High-order spectral element for elastic wave modeling," Abstracts of the 62nd Annual International SEG Meeting, New Orleans, Louisiana, Soc. Expl. Geophys., 1285–1288 (1992).
[19] T. Hughes, *The Finite Element Method* (Prentice-Hall, Englewood Cliffs, NJ, 1987).
[20] O. Axelsson and V. A. Barker, *Finite-Element Solution of Boundary Value Problems (Theory and Computation)* (Academic, London, 1984).
[21] De Hoop, "Modification of Cagniard's method for solving seismic pulse problems," Appl. Sci. Res. B **8**, 349–356 (1960).
[22] A. Ben-Menahem and S. J. Singh, *Seismic Waves and Sources* (Springer-Verlag, New York, 1981).
[23] K. Aki and P. Richards, *Quantitative Seismology* (Freeman, San Francisco, CA, 1980).
[24] M. Ottaviani, "Elastic wave propagation in two evenly-welded quarter-spaces," Bull. Seismol. Soc. Am. **59**, 1119–1152 (1971).
[25] E. R. Lapwood, "The transmission of a Rayleigh pulse round a corner," Geophys. J. **4**, 174–196 (1961).
[26] J. C. de Bremaecker, "Transmission and reflection of Rayleigh waves at corners," Geophysics **23**, 253–266 (1958).
[27] L. Knopoff and A. F. Gangi, "Transmission and reflection of Rayleigh waves by wedges," Geophysics **25**, 1203–1214 (1960).
[28] J. M. Carcione, "A 2-D Chebyshev differential operator for the elastic wave equation," Comput. Methods Appl. Mech. Eng. (submitted).
[29] J. M. Carcione, "Domain decomposition for wave propagation problems," J. Sci. Comput. **6**, 453–472 (1991).
[30] J. M. Carcione and J. P. Wang, "A Chebyshev collocation method for the wave equation in generalized coordinates," in *Proceedings of the Second International Conference on Mathematical and Numerical Aspects of Wave Propagation*, Newark, Delaware, edited by R. Kleinman, D. Colton, F. Santosa, and I. Stakgold (SIAM, Philadelphia, 1993), pp. 128–137.
[31] B. A. Auld, "Rayleigh wave propagation," in *Rayleigh-Wave Theory and Applications*, edited by E. A. Ash and E. G. S. Paige (Springer-Verlag, New York, 1985), pp. 12–28.
[32] B. Rulf, "Rayleigh waves on curved surfaces," J. Acoust. Soc. Am. **45**, 493 (1968).
[33] Lord Rayleigh, "Whispering galleries," in *The Theory of Sound 2* (MacMillan, London, 1896), 2nd ed., Sec. 287, p. 126.